Volume 7
Number 11
7 June 2025
Pages 3147–3590

Nanoscale Advances

rsc.li/nanoscale-advances

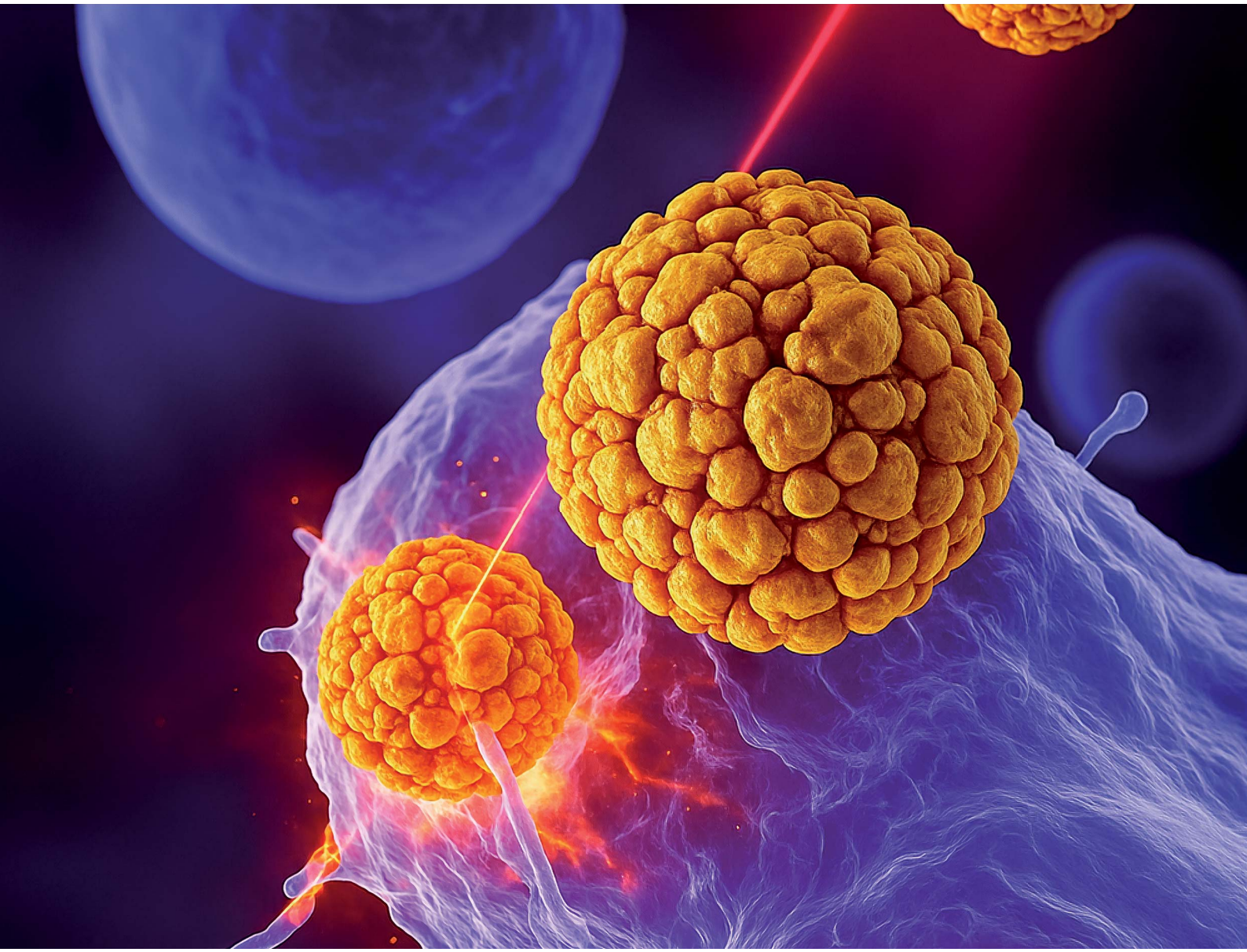

ISSN 2516-0230

ROYAL SOCIETY OF CHEMISTRY

PAPER

Miguel Monge, José M. López-de-Luzuriaga *et al.*
An organometallic approach to sub-2 nm thiolate-protected Au nanoclusters with enhanced catalytic and therapeutic properties

NCNST

Nanoscale Advances

ROYAL SOCIETY OF CHEMISTRY

PAPER

View Article Online
View Journal | View Issue

Cite this: *Nanoscale Adv.*, 2025, **7**, 3228

An organometallic approach to sub-2 nm thiolate-protected Au nanoclusters with enhanced catalytic and therapeutic properties†

Irene del-Campo, [a] Alba Sorroche, [a] Nina Allen,[b] Mattia Ghirardello,[ac] Francisco Corzana, [a] M. Carmen Galán, [b] Miguel Monge *[a] and José M. López-de-Luzuriaga *[a]

Received 5th February 2025
Accepted 16th April 2025

DOI: 10.1039/d5na00123d

rsc.li/nanoscale-advances

Thiolate-protected gold nanoclusters (AuNCs) of sub-2 nm size have been synthesized through a novel bottom-up approach using the organometallic precursor [Au(C_6F_5)(tht)] (tht = tetrahydrothiophene) in a one-pot reaction under mild conditions. This protocol is simple, rapid (1 h), versatile (applicable to thiolate ligands of varying molecular sizes), and reproducible, yielding AuNCs with low size dispersion. Furthermore, the resulting nanomaterials exhibited remarkable catalytic activity, effectively reducing the pollutant 4-nitrophenol to 4-aminophenol, as well as promising photothermal and photodynamic properties upon exposure to an 808 nm laser, converting light into thermal energy and generating reactive oxygen species (ROS). Additionally, AuNCs stabilized with a nonapeptide demonstrated efficient catalase-like activity, thereby potentially enhancing the efficacy of photodynamic therapy. The cytotoxic effects against cancer (HeLa) and healthy cells (HDF) were also evaluated, showing greater selectivity for HeLa cells, with higher toxicity and increased ROS generation.

Introduction

Gold nanoclusters (AuNCs) constitute a class of nanomaterials characterized by particle sizes below 2 nm and exhibit unique physicochemical properties. AuNCs are composed of an inorganic core containing a few to hundreds of gold atoms, and an outer shell of molecules which is required to prevent aggregation. The latter also defines their ability to be suspended in solution and can be tuned *via* functionalization for different applications. A variety of organic ligands have been employed for this purpose, including thiolates,[1–4] phosphines[5,6] carbenes,[7,8] alkynes[9,10] and selenolates.[11,12] Among those, thiolates have been intensively studied due to the ease of preparation and the strong S–Au bonds, which provide excellent stability in solution.[13,14]

Due to their small size, situated between single atoms and gold nanoparticles (AuNPs), AuNCs exhibit quantum confinement effects that cause the continuous energy bands to break up into discrete energy levels. As a consequence of their size, the physicochemical properties of AuNCs differ significantly from those of AuNPs. While AuNPs exhibit an optical phenomenon called Localized Surface Plasmon Resonance (LSPR), which arises from the resonant collective oscillation of electrons in the conduction band with incident light, AuNCs do not display this phenomenon due to their distinct electronic characteristics. These differences also lead to tunable luminescence,[15,16] HOMO–LUMO electronic transitions,[17,18] quantized charge, magnetism,[19] molecular chirality[20] and different absorption peaks.[21] Moreover, AuNCs possess a high specific surface area-to-volume ratio and a large number of unsaturated reaction sites, which result in higher catalytic activities than that of AuNPs and unique selectivity in catalytic reactions such as oxidation, hydrogenation and C–C coupling, including photocatalysis and electrocatalysis.[22–24] In addition, AuNCs are very promising for biomedical applications such as radiotherapy,[25] photothermal therapy,[26] photodynamic therapy,[27] theranostics and drug delivery[28] due to their non-toxicity, better cell membrane penetration and enhanced excretion.[29]

In general, the use of organometallic complexes as precursors for the synthesis of nanomaterials offers the possibility to work under mild conditions and presents several advantages for the production of well-controlled nanostructures in terms of size dispersion, chemical composition, shape and organization.[30] Furthermore, our research has focused on the controlled preparation of sub-10 nm size Au and/or Ag nanostructures

[a]*Department of Chemistry, Instituto de Investigación en Química de la Universidad de La Rioja (IQUR), Universidad de La Rioja, Logroño, 26006, Spain. E-mail: miguel.monge@unirioja.es; josemaria.lopez@unirioja.es*

[b]*United Kingdom School of Chemistry, University of Bristol, Cantock's Close, BS8 1TS, UK*

[c]*Institute for Biocomputation and Physics of Complex Systems (BIFI), University of Zaragoza, Zaragoza, 50018, Spain*

† Electronic supplementary information (ESI) available: Materials, methods, additional experimental details (HAADF-STEM, XPS, and UV-vis), additional results and supplementary references. See DOI: https://doi.org/10.1039/d5na00123d

through the mild decomposition of pentafluorophenyl-based gold(I) and/or silver(I) precursors.[31–33]

The most common strategy in bottom-up synthesis of thiolate-protected gold nanoclusters (AuNCs–SR) consists in the chemical reduction in solution of Au(III) salts, typically $HAuCl_4$. The use of an excess of thiolate ligands is frequently employed to convert the nanoclusters into monodisperse ones *via* thermodynamic control.[13] In this report, we describe a simple and efficient organometallic approach for the synthesis of AuNCs–SR, using a Au(I) precursor, which is [Au(C_6F_5)(tht)] (tht = tetrahydrothiophene), instead of an Au(III) salt. The reaction conditions employed in this study have yielded thiolate-protected sub-2 nm size gold nanoclusters. A narrow size distribution has been achieved under mild conditions in a simple, rapid and reproducible organometallic method. It is noteworthy that this method represents a significant advancement in the field, as prior to this development thiolate-protected AuNCs had not been obtained with gold organometallic precursors. The addition of a mild reducing agent, triisopropylsilane (TIPS), and a peptide ligand as a stabilizing agent enabled the rapid synthesis of the desired AuNCs at room temperature.

In this study, cysteine (Cys), glutathione (GSH) and a 9-amino acid oligopeptide (pep9) were employed as thiolated capping agents with the objective of evaluating the versatility of the method by using water-soluble ligands of different atomic lengths. As a biologically relevant biomolecule, a nonapeptide was selected based on a region of mucin-1 (MUC1), an *O*-glycosylated glycoprotein whose extracellular domain consists of a tandem repeat of 20 amino acids (HGVTSAPDTRPAPG-STAPPA) and is overexpressed in tumour cells. We selected the MUC1 peptide fragment pep9, with the sequence CAPDTRPAP as the protective ligand equipped with a N-terminal Cys residue to facilitate the AuNC functionalization. With MUC1-based vaccines under development to elicit robust immune responses, the selection of pep9 represents the initial step in assessing the potential of AuNCs for biomedical applications.[34] Additionally, we present the characterization of these AuNCs, alongside initial studies of their catalytic and therapeutic properties.

Experimental

Complementary information is given in the ESI† (furnishers, materials, methods, synthesis of precursors, and additional experimental details).

Synthesis of AuNCs (1), (2), and (3)

In a typical synthesis, 2600 μL of THF and 100 μL of [Au(C_6F_5)(tht)] 50 mM THF freshly prepared solution were added to a flask. Subsequently, 3000 μL of ultrapure water was added, and immediately after, while stirring vigorously at room temperature, 15 μL of TIPS (14.6 equiv.) were added. This resulted in the formation of a turbid, orange-brown solution within seconds. After 1 min of stirring, 200 μL of an aqueous 50 mM ligand solution (for AuNCs–Cys (**1**) and AuNCs–GSH (**2**)) or 100 μL of aqueous 50 mM nonapeptide (AuNCs–pep9 (**3**)) were added, changing the brown shade of the solution (see ESI, Fig. S3†). The solution was stirred for 1 hour at room temperature. The sample containing GSH presented a darker colour than that in the case of Cys, both showing a brownish precipitate. On the other hand, the lack of precipitates and a lighter brown colour was observed in AuNCs–pep9 (**3**) solution.

Catalysis: reduction of 4-nitrophenol to 4-aminophenol

2.5 mL of ultrapure H_2O, 100 μL of 2.5 mM 4-nitrophenol and 150 μL of a freshly prepared 1 M $NaBH_4$ solution were added to a quartz cuvette, giving rise to an intense yellow solution. 30 μL of the catalyst, as-synthesized and diluted in water, was then added (Au at 0.01 equiv. of 4-NP).

Photothermal effect

1 mL of the corresponding AuNC solution (0.85 mM in H_2O : THF 1.2 : 1) was added to a 2 mL vial and irradiated from above using an 808 nm laser (2.5 W cm^{-2}). Temperature changes were monitored using a FLIR E6-XT thermographic camera.

$^1O_2$ generation

In every experiment, 1844 μL of acetonitrile (air bubbled), 38.6 μL of H_2O_2 (30%), 817 μL of the 0.85 mM catalyst and 300 μL of a freshly prepared solution of DPBF 600 μM were added. It was irradiated from above using an 808 nm laser (2.5 W cm^{-2}). For the control experiment, 817 μL of the H_2O : THF (1.2 : 1) solvent mixture were added instead of the catalyst. For the catalyst reuse study, 300 μL of DPBF (600 μM) and 38.6 mL of H_2O_2 (30%) were added every 30 min.

Cell culture

Unless otherwise specified, cells were incubated at 37 °C in a 5% CO_2 atmosphere. HeLa cells were cultured in Dulbecco's Modified Eagle Medium with 4.5 g per L glucose, 10% FBS, and a Gibco™ antibiotic–antimycotic cocktail. HDF cells were cultured in minimum essential media with 10% FBS and a Gibco™ antibiotic–antimycotic cocktail.

Cytotoxicity study

HeLa cells (2×10^4) or HDF cells (2×10^5) were seeded in 96-well plates and incubated with increasing concentrations of each ligand (0–250 μg mL^{-1}), with at least 4 repeats of each sample. After 2 hours of incubation, the cells were irradiated (855 nm) at RT for 1–2 hours, or kept in the dark at RT for 2 hours. After a further 24 h of incubation the medium was removed and the cells were washed twice with PBS. AlamarBlue™ solution (5% v/v, Thermo Fisher Scientific) in FBS-free media (100 μL) was then added and cells were incubated for 2 h at 37 °C. AlamarBlue fluorescence (λ_{ex} = 555 nm, λ_{em} = 590 nm) was then measured using a CLARIOstar plate reader and cell viability was determined as a percentage of the untreated control cells. Dose response (inhibition) curves were plotted in GraphPad Prism using non-linear regression to determine EC_{50} values.

ROS production

HeLa or HDF cells (2×10^5) were seeded in 96-well plates and incubated with or without ligands (100 μg mL^{-1}) for 2 hours, with 8 repeats of each sample. The cells were incubated for 2 hours at 37 °C, and then irradiated at 855 nm at RT for 1 hour, or kept in the dark at RT for 1 hour. The medium was then removed and the cells were washed twice with PBS. Dihydroethidium solution (1 mg mL^{-1} in PBS, 100 μL) was then added to each well, incubated for 15 minutes at 37 °C and then the fluorescence was measured (λ_{ex} = 520 nm and λ_{em} = 590 nm) using a CLARIOstar plate reader.

Results and discussion

Synthesis and characterization of gold nanoclusters

Thiolate-protected gold nanoclusters (AuNCs–SR) were synthesized by adding triisopropylsilane (TIPS) as a reducing agent to a solution of the organometallic precursor [Au(C_6F_5)(tht)] in a mixture of THF and ultrapure water under magnetic stirring. After a few seconds, a turbid dark brown mixture was obtained. Subsequently, a stabilizing agent was added, resulting in a change in the brown shade of the solution (Fig. S3†). The reduction to Au(0) was evidenced by the change in colour from colourless to dark brown. Cys, GSH and pep9 were employed as surface-protecting ligands, leading to nanomaterials AuNCs–Cys (**1**), AuNCs–GSH (**2**) and AuNCs–pep9 (**3**), respectively (Scheme 1).

High-Angle Annular Dark-Field Scanning Transmission Electron Microscopy (HAADF-STEM) micrographs of AuNCs (Fig. 1A, B and S4–S6†) demonstrate the presence of a main population of homogeneously distributed gold nanoclusters, with average diameters of 1.1 ± 0.5 nm for AuNCs–Cys (**1**), 1.9 ± 0.6 nm for AuNCs–GSH (**2**) and 1.8 ± 0.6 nm for AuNCs–pep9 (**3**) (Fig. S7–S9†). These results suggest that the method developed in this work mainly provides gold nanoclusters with minimal amounts of small nanoparticles and exhibits a stabilizing agent-dependence on their size and distribution. The reduced size of AuNCs–Cys (**1**) could be attributed to an increased number of ligands on the surface, which prevents gold aggregation, thanks to the smaller size of the ligands.

The presence of AuNCs was also confirmed through UV-vis absorption and X-ray Photoelectron Spectroscopy (XPS) measurements (Fig. 1C and D). The UV-vis spectra showed a strong absorption at high energies and an exponential decay, as previously observed in the literature for gold nanoclusters.[26] Furthermore, the lack of a plasmon band would indicate that nanoparticles were practically absent, which would be in agreement with the presence of AuNCs less than 2 nm in size.

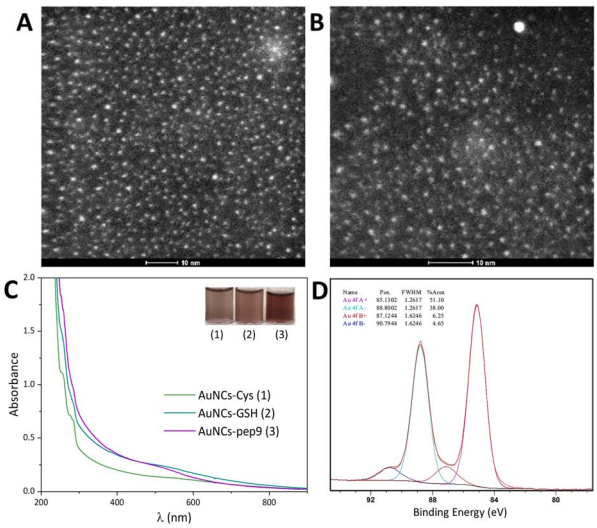

Fig. 1 Characterization of AuNCs: (A) HAADF-STEM image of AuNCs–Cys (**1**). (B) HAADF-STEM image of AuNCs–GSH (**2**). (C) UV-vis absorption spectra. (D) High-resolution Au 4f XPS spectrum of AuNCs–Cys (**1**).

The general XPS spectrum (Fig. S10†) showed the elements present on the nanomaterials in addition to Au: C, S, O and N were present due to ligands, and fluorine atoms were also identified, which could indicate the presence of $C_6F_5^-$ to some extent on the surface, potentially contributing to enhancement of the AuNC colloidal stability. The atomic composition revealed an Au : S ratio of 1 : 1.85 for AuNCs **1**, 1 : 0.97 for AuNCs **2** and 1 : 1.56 for AuNCs **3**. The lowest amount of sulfur observed for AuNCs **2** could be attributed to the fact that in glutathione, which is composed of a tripeptide (Glu–Cys–Gly), the Cys residue occupies a central position, which would result in steric hindrance and a reduction in the number of ligands present on the surface. The Au 4f XPS spectra of the three AuNCs (Fig. 1D

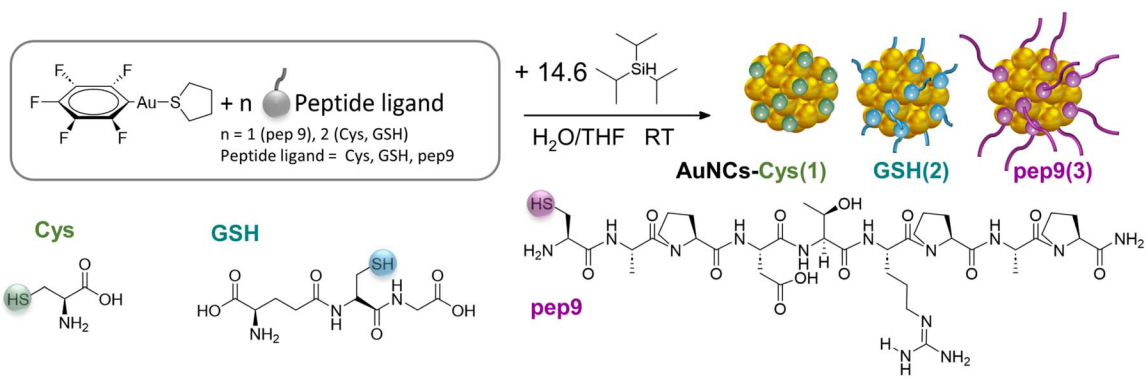

Scheme 1 Synthesis of AuNCs–Cys (**1**), –GSH (**2**) and –pep9 (**3**).

and S11†) exhibited peaks that can be deconvoluted into two spin–orbit doublets with different intensities but the same energy separation (ΔE = 3.7 eV), which originated from the inner and surface atoms of the AuNCs. The most intense doublet (89–92%) was attributed to Au(0), located at higher energy compared with bulk gold (87.4 and 84.0 eV). The XPS gold peaks demonstrated a positive shift, in accordance with previously reported thiolate-protected AuNCs,[35–37] as the Au 4f peaks sensitively shift to higher binding energy when the size of AuNCs decreases.[38] The majority composition of Au(0) would indicate an effective reduction of the metal centre caused by TIPS. The second doublet (11–8%) was attributed to $Au^{\delta+}$ charged atoms,[39] corresponding to the surface Au components, at a higher energy than the inner components since the electron donation occurs from the surface Au atoms to the thiolates.[35]

The effective coordination of the thiolate ligands on the gold nanoclusters was confirmed by FT-IR spectroscopy and ^{1}H NMR analysis. The FT-IR spectra of the three AuNCs exhibited characteristic vibrational bands corresponding to the stabilizing ligands Cys, GSH and pep9, indicating a successful binding (Fig. S12–S14†). Furthermore, the ^{1}H NMR spectrum of the centrifuged sample of AuNCs **3** revealed broadening of the signals associated with the stabilizing peptide (Fig. S15†), consistent with this type of system. When molecules are attached to a metal nanoparticle, line broadening of the resonances is observed, the chemical shift may be altered, and some resonances may disappear completely.[40] These findings provide strong evidence for the incorporation of the nonapeptide as a capping ligand.

Catalytic activity: reduction of 4-nitrophenol to 4-aminophenol

AuNCs have garnered significant attention in catalysis due to their unique physical properties. Their high reactivity and large surface-to-volume ratio, a consequence of their ultra-small size, make them particularly attractive for catalysis applications. In order to evaluate their catalytic performance, the reduction of 4-nitrophenol (4-NP) to 4-aminophenol (4-AP) was selected as a model reaction for comparison studies. To evaluate the catalytic conversion, we monitored the absorbance decrease of the band attributed to the 90 μM 4-nitrophenolate ions (410 nm) in water at room temperature with 1.0% of the catalyst (Fig. 2A, S17 and S18†).

In all experiments, an excess of $NaBH_4$ (600 equiv.) was added to ensure pseudo-first-order kinetics. However, in these three cases it was observed that the representation of $\ln(A_t/A_0)$ *vs.* time did not fit a single straight curve (Fig. 2B), indicating that the kinetics were more complex. For the purposes of facilitating analysis and comparison, the data have been treated as two first-order curves with different slopes.

The initial slope showed apparent kinetic constants k_{app} of 0.39, 0.43, and 0.88 min^{-1} for AuNCs **1**, **2**, and **3**, respectively. The second linear trend exhibited a greater slope than the first (0.58, 0.87 and 1.53 min^{-1}), indicating that a modification occurred on the surface of the catalyst during the reaction that enables enhanced interaction and favoured catalysis.

Based on these observations, it can be hypothesized that the presence of an excess of $NaBH_4$ could result in the reduction of some of the stabilizing agents on the catalyst surface, thus

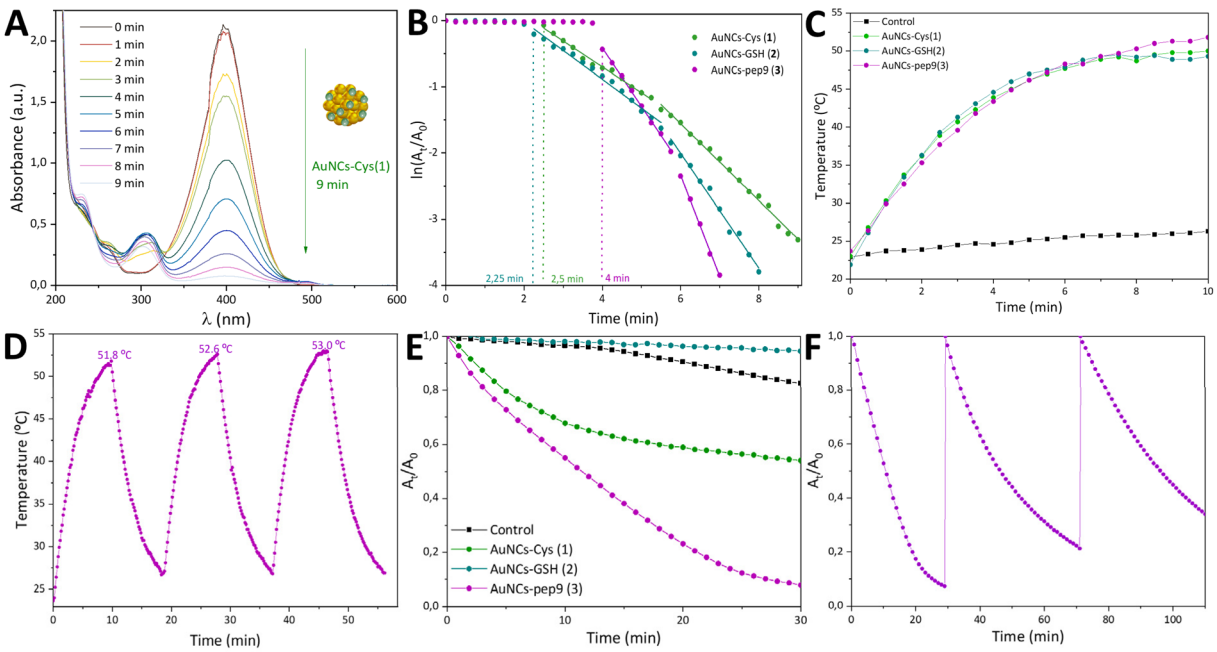

Fig. 2 (A) UV/vis monitored reduction of 4-NP to 4-AP (reaction conditions: 90 μM 4-NP in water at room temperature, 1.0% of the catalyst, 600 equivalents of $NaBH_4$) with AuNCs–Cys (**1**) as the catalyst. (B) $\ln(A_t/A_0)$ of the peak intensity at 400 nm as a function of time in the reduction of 4-NP to 4-AP. (C) Photothermal heating curves for solvent and 0.85 mM AuNCs (**1**, **2**, and **3**) under NIR laser light (808 nm, 2.5 W cm^{-2}). (D) On–off NIR laser irradiation cycles for AuNCs–pep9 (**3**) under NIR laser light (808 nm, 2.5 W cm^{-2}). (E) Absorbance decay of DPBF measured at 410 nm for solvent and AuNCs (**1**, **2**, **3**) in the $^1O_2$ generation reaction (60 μM DPBF, 0.23 mM Au, 125 mM H_2O_2). (F) Three cycles of absorbance decay measured at 410 nm using AuNCs **3** in the $^1O_2$ generation reaction.

generating free thiol ligands. This would increase the accessibility of the metal surface, enhancing the adsorption of both hydrogen and 4-NP, and therefore, improving catalytic performance, as previously demonstrated in the literature.[41] The time-resolved ^{1}H NMR spectra of the reaction between AuNCs–Cys (**1**) and $NaBH_4$ support this hypothesis (see ESI, Fig. S19†), showing that the reductant is capable of liberating cysteine from the surface, which contributes to the increased catalytic efficiency of AuNCs during the reaction.

The induction time (t_0) showed a stabilizing ligand dependence: AuNCs **3** exhibited a longer induction time (4 min), possibly due to the steric hindrance caused by the greater ligand volume, which would hinder surface reduction and the initial adsorption step. In contrast, the catalytic reaction with AuNCs **1** and **2**, which were stabilized by smaller ligands, resulted in shorter induction times (2.5 and 2.25 min, respectively). This suggests that reductive desorption occurs more rapidly with shorter ligands, which also facilitate hydrogen transfer to the catalyst, promoting its activation. The calculated kinetic constant values also suggest an increasing trend: larger ligand volumes resulted in higher values (Table 1). Although the reduction is more effective for smaller ligands, as evidenced by the shorter induction times, it has also been demonstrated that the presence of borohydride increases the dimensions of the nanoclusters.[41] Larger nanoparticles are formed as a consequence, and thus a higher volume of the capping ligand could prevent the aggregation of AuNCs and result in a higher number of catalytic sites available.

In order to evaluate the quality of our results we have compared them to previously reported ones in Table 1. The nanomaterials generated in this work showed superior catalytic performance in the reduction of 4-NP in comparison to other AuNCs. The use of dimethylformamide-stabilized gold nanoclusters (AuNCs–DMF) with the same gold ratio and an increased quantity of $NaBH_4$ resulted in a lower rate constant (0.18 min^{-1}). The same situation occurred with AuNCs stabilized with alkanethiolates ($C_{18}SH$, $C_{12}SH$, and C_6SH), with lower values of k_{app} using 100-fold more catalyst and a higher excess of sodium borohydride, indicating a better performance for the AuNCs in the present study.[41]

Table 1 Comparison of the catalytic performance of AuNCs–SR[a]

Sample	% Au	$NaBH_4$ [eq.]	k_{app} (min^{-1})
AuNCs–Cys (**1**)	1.0	600	0.39–0.58
AuNCs–GSH (**2**)	1.0	600	0.43–0.87
AuNCs–pep9 (**3**)	1.0	600	0.88–1.53
AuNCs–DMF[42]	1.0	2000	0.18
AuNCs–$C_{18}SH$[41]	100	1000	0.28
AuNCs–$C_{12}SH$[41]	100	1000	0.31
AuNCs–C_6SH[41]	100	1000	0.35
$Au_{25}(GSH)_{18}$ NCs[42]	1.0	2000	0.48
$Au_{25}(MPA)_{18}$ NCs[43]	28	Excess	4.8
$Au_{25}(MUA)_{18}$ NCs[43]	28	Excess	0.42
$Au_{25}(p\text{-}MBA)_{18}$ NCs[43]	28	Excess	3.9
AuNPs–CTAB (3.5 nm)[44]	6.3	500	0.072
AuNPs–DHBC (10 nm)[45]	5.0	300	0.77

[a] Experimental: 4-NP in water at room temperature monitored by UV-vis.

On the other hand, AuNCs **1**, **2** and **3** also showed better catalysis results than atomically precise nanoclusters. For instance, $Au_{25}(GSH)_{18}$ NCs and $Au_{25}(MUA)_{18}$ NCs exhibited a k_{app} of 0.48 and 0.42 min^{-1}, respectively, indicating lower catalytic conversions.[42,43] The catalytic constants for $Au_{25}(MPA)_{18}$ NCs and $Au_{25}(p\text{-}MBA)_{18}$ NCs were found to be higher (4.8 and 3.9 min^{-1}) with the use of a greater quantity of gold and higher excess of $NaBH_4$.[43] Additionally, a comparison of the catalytic activity of AuNCs and small gold nanoparticles is crucial since the presence of an excess of the reductant tends to aggregate the nanoclusters and give rise to nanoparticles. The catalytic rates obtained in this study were higher than those observed for small AuNPs stabilized with cetyltrimethylammonium bromide (CTAB).[44] Furthermore, AuNCs **2** and AuNCs **3** demonstrated superior performance compared to 10 nm AuNPs stabilized with a double hydrophilic block copolymer (DHBC).[45]

Photothermal properties

Gold nanomaterials are very promising photothermal agents due to their great ability to convert near-infrared (NIR) radiation into thermal energy. The mechanisms of the photothermal conversion processes of AuNCs can be attributed to molecular vibrations, due to their molecular-like properties and the absence of plasmonic localized vibrations. After the relaxation of the excited electrons to the ground state through vibration-electron coupling, the excess energy is released in the form of heat.[46]

To examine the photothermal properties, AuNCs **1**, **2** and **3** were irradiated using an 808 nm NIR laser (2.5 W cm^{-2}). In this study, it was observed that for the three nanomaterials, there was a noticeable change in temperature under irradiation, increasing by more than 25 °C for a 170 μg per mL gold concentration (Fig. 2C). The irradiation of the solvent (mixture of H_2O with THF) caused a slight increase in temperature of less than 4 °C, suggesting that the nanoclusters of this work were capable of converting NIR light into thermal energy, proving their possible usefulness in photothermal therapy. Considering the intrinsic error of measurement, the nanoclusters of this work showed similar photothermal properties with no noticeable stabilizing ligand-dependence. The photothermal properties of AuNCs **1**, **2** and **3** were comparable to those of other nanoclusters reported in the literature. For example, at a slightly reduced power density of 2.0 W cm^{-2}, DNase–AuNCs (225 μg mL^{-1})[47] and $Au_{25}(Capt)_{18}$ (200 μg mL^{-1})[48] reached 41 and 46 °C, respectively, within a five-minute period.

We also wanted to study the photothermal stability to verify the reusability of the system, crucial for possible practical applications. AuNCs–pep9 (**3**) was selected for this study, as it showed higher solubility in water and good photothermal properties. Three thermal conversion cycles were conducted (Fig. 2D), resulting in a temperature higher than 51 °C in all of them. Therefore, nanomaterial **3** maintained the ability to convert radiation into heat through the different cycles, showing good stability.

Photodynamic activity

Photodynamic therapy (PDT) is a promising approach for cancer treatment that utilized a photosensitizer to absorb light and generate reactive oxygen species (ROS), such as free radicals or singlet oxygen ($^1O_2$), which induces cell toxicity and damage. When combined with photothermal therapy, PDT offers enhanced therapeutic efficacy, providing a more powerful strategy.

In addition to its role in PDT, AuNCs can exhibit catalase-like activity, enabling the conversion of hydrogen peroxide into oxygen, and, consequently, enhancing the effectiveness of PDT. This process helps to overcome the challenges of hypoxia in tumour environments, characterized by high levels of H_2O_2 and low levels of O_2.[49,50]

To assess $^1O_2$ generation, we used 1,3-diphenylisobenzofuran (DPBF) as an $^1O_2$ scavenger under 808 nm laser irradiation (2.5 W cm^{-2}) and evaluated the catalase-like activity by monitoring the absorbance decay of DPBF in the presence of H_2O_2 (Fig. 2E). The control experiment resulted in a 17% decay in 30 minutes since DPBF also reacts with H_2O_2 and is unstable and sensitive to external factors such as UV light and heat. The use of AuNCs–pep9 (**3**) under the same conditions resulted in a 92% reduction in DPBF absorbance within 30 minutes, which would differ significantly from the control experiment. Differences in behaviour were observed for nanomaterials AuNCs–Cys (**1**) and AuNCs–GSH (**2**): for AuNCs **1**, the initial slope was greater than that of the control experiment, while for AuNCs **2** and the second slope of AuNCs **1**, a lower decay rate was shown. These observed differences could be explained considering the stability of the nanoclusters (Fig. S21†). During the experiment, the decomposition of the catalysts AuNCs–Cys (**1**) and AuNCs–GSH (**2**) was observed, leading to the formation of aggregates and insoluble particles. In contrast, AuNCs–pep9 (**3**) maintained its stability, with the solution remaining a transparent brownish colour throughout the experiment. The enhanced stability of AuNCs **3** in the reaction medium, in comparison to its analogues with Cys (**1**) and GSH (**2**), enabled an effective photodynamic effect under NIR light irradiation.

The catalase-type activity of AuNCs **3** was confirmed through measurements conducted in the absence of H_2O_2 (Fig. S22†) under laser irradiation, demonstrating its capacity for solving the problem of hypoxia, which severely limits PDT. Owing to DPBF being sensitive to heat, to ensure that its degradation was attributable to the presence of $^1O_2$ and not a consequence of photothermal heat generated by the nanoclusters, the final temperatures were verified (Table S2†). As the temperature increase observed in the three AuNCs was almost identical, it can be assumed that the observed differences in behaviour were not a result of the temperature variations.

Lastly, since AuNCs **3** has presented good photodynamic properties and photothermal stability, the reusability of the catalyst in the $^1O_2$ generation reaction was verified through three cycles. The results showed a complete conversion of the DPBF compound in the first cycle and a reduced catalytic power in the new cycles, showing a small loss in their $^1O_2$ generation capacity but also indicating the ability of the nanomaterial to be reused (Fig. 2F).

Cytotoxicity study

In order to evaluate the biocompatibility of the gold nanoclusters, the cytotoxic properties of the AuNCs–Cys (**1**) and AuNCs–pep9 (**3**) against healthy cells (HDF) and cancer cells (HeLa) were examined in the absence and presence of NIR light, to assess their potential application in photothermal and/or photodynamic therapy.

Production of reactive oxygen species (ROS) in live cells was assessed using a dihydroethidium fluorescence assay (Fig. 3). Minimal ROS production was observed in the dark for AuNCs **1** and **3** in treated HeLa and HDF cells, suggesting that the nanoclusters themselves do not exhibit significant toxicity in the absence of irradiation. Under NIR irradiation (855 nm), AuNCs **1** and **3** exhibited higher ROS production in the cancer cell line, with no equivalent increase in ROS production for the healthy cell line, highlighting the potential for selective killing of cancer cells *via* ROS production.

To determine the cytotoxicity of the AuNCs, cells were incubated with AuNCs **1** and **3** (0–250 μg mL^{-1}), respectively, for 2 h and either kept in the dark for a further 2 h or irradiated at 855 nm for 1 or 2 h. The cytotoxicity was then assessed using an alamarBlue fluorescence assay at 24 hours post-treatment (Fig. S23†). The results (Table 2) indicate that in the dark, AuNCs **3** showed higher toxicity in HeLa cells (100–250 μg mL^{-1}) than HDF cells (>250 μg mL^{-1}), while AuNCs **1** exhibited comparable toxicity for both cell lines (50–100 μg mL^{-1}). In AuNCs **3** treated HeLa cells, NIR irradiation (855 nm, for 1 or 2 h) induced higher toxicity (50–100 μg mL^{-1}) than cells kept in the dark (100–250 μg mL^{-1}) when compared to untreated controls, while exposure to AuNCs **1** showed comparable toxicity irrespective of NIR irradiation (50–100 μg mL^{-1}). In HDF cells, NIR irradiation did not increase toxicity for AuNCs **3** treated cells, and decreased toxicity for AuNC **1** treated cells. No toxicity was observed for pep9 with either cell line in the dark or under NIR irradiation. These findings suggest that AuNCs **3** may be more promising for selective photothermal and photodynamic therapy, as they display a stronger therapeutic effect in cancer cells under NIR irradiation while showing minimal toxicity to healthy cells.

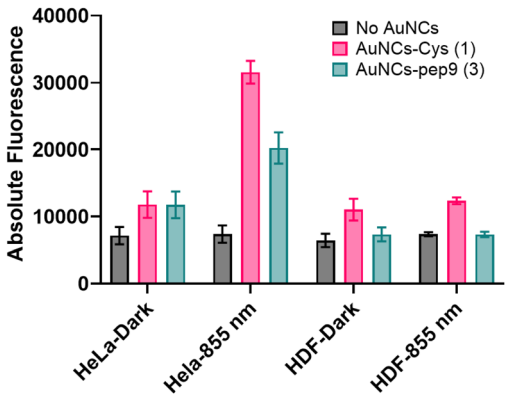

Fig. 3 Cytotoxicity study of AuNCs **1** and **3** against healthy (HDF) and cancer cell (HeLa) : ROS production using an 855 nm lamp.

Table 2 IC_{50} values of pep9, AuNCs–Cys (**1**) and AuNCs–pep9 (**3**) against HDF and HeLa cells

		Approx. IC_{50}/μg mL^{-1}		
		Pep9	AuNCs–Cys (**1**)	AuNCs–Pep9 (**3**)
HDF (healthy)	Dark	>250	50–100	>250
	1 h – 855 nm	>250	>250	>250
	2 h – 855 nm	>250	>250	>250
HeLa (cancer)	Dark	>250	50–100	100–250
	1 h – 855 nm	>250	50–100	50–100
	2 h – 855 nm	>250	50–100	50–100

The XPS data indicated that the atomic gold percentage of AuNCs **1** was higher than that of AuNCs **3** (3.27% and 0.48%, respectively), as would be expected when using a stabilising ligand (Cys) of lower molecular mass. As the toxicity was attributable to gold, it can be postulated that the cytotoxic properties observed for AuNCs **3** were diminished in comparison to those of AuNCs **1**. However, even with a lower overall gold content, AuNCs **3** provided a more targeted and effective treatment in cancer cells, with the potential for reduced toxicity in healthy cells due to their selectivity. This fact is particularly advantageous for therapeutic applications, as it could minimize side effects.

Conclusions

This study introduces an efficient and consistent approach for synthesizing thiolate-protected gold nanoclusters with sizes under 2 nm, achieved through the reduction of an organometallic precursor under mild conditions. The synthesis method is rapid, offers excellent size control, and is versatile, as it can be successfully applied with various thiol-based stabilizing agents. This approach consistently produces gold nanoclusters with promising properties, including high catalytic activity and favourable photothermal and photodynamic characteristics, which can be tuned by selecting different thiol ligands. The cytotoxicity evaluation revealed greater selectivity against cancer cells compared to healthy cells when using the nonapeptide pep9 as the stabilizing agent, which also enhanced ROS production. This organometallic-based methodology establishes a new synthesis method for the development of thiolate-protected gold nanoclusters, with interesting prospects for both biological and catalytic applications. Further research is underway to integrate other biologically relevant thiol-containing agents, taking advantage of the versatility of this method.

Data availability

The data supporting this article have been included as part of the ESI.†

Conflicts of interest

There are no conflicts to declare.

Acknowledgements

We acknowledge the DGI MICINN/FEDER (project number PID2022-139739NB-l00 and PID2021-127622OB-I00) co-funded by the European Regional Development Fund (ERDF) "A way of making Europe". I. del-Campo also aknowledges MICIU for a FPU grant. MCG and NA thank EPSRC TECS CDT EP/S024107/1 and the EP/S026215/1. Project has received funding from the European Union's Horizon 2020 research and innovation program under grant agreement no. 101034288 (an innovation programme under the Marie Skłodowska-Curie COFUND grant agreement). MG acknowledges the Foundation of the Spanish Association Against Cancer for supporting this work. The authors also acknowledge the use of instrumentation as well as the technical advice provided by the National Facility ELECMI ICTS, node "Laboratorio de Microscopias Avanzadas" at the Universidad de Zaragoza.

References

1 A. Deák, P. T. Szabó, V. Bednaříková, J. Cihlář, A. Demeter, M. Remešová, E. Colacino and L. Čelko, *Front. Chem.*, 2023, **11**, 1178225.
2 H.-Y. Chang, Y.-T. Tseng, Z. Yuan, H.-L. Chou, C.-H. Chen, B.-J. Hwang, M.-C. Tsai, H.-T. Chang and C.-C. Huang, *Phys. Chem. Chem. Phys.*, 2017, **19**, 12085–12093.
3 H. Huang, G. B. Hwang, G. Wu, K. Karu, H. D. Toit, H. Wu, J. Callison, I. P. Parkin and A. Gavriilidis, *Chem. Eng. J.*, 2020, **383**, 123176.
4 J. S. Kim, N. Park, S. J. Kwak, Y. Jeon, G. Lee, Y. Kim, W. B. Lee and J. Park, *ACS Nano*, 2024, **18**, 14244–14254.
5 J. M. Pettibone and J. W. Hudgens, *Phys. Chem. Chem. Phys.*, 2012, **14**, 4142.
6 S. Jin, W. Du, S. Wang, X. Kang, M. Chen, D. Hu, S. Chen, X. Zou, G. Sun and M. Zhu, *Inorg. Chem.*, 2017, **56**, 11151–11159.
7 J. Sun, X. Tang, J. Tang, Y. Zhang, Z. Li, Chaolumen, S. Guo and H. Shen, *Inorg. Chem.*, 2023, **62**, 5088–5094.
8 Q. Wu, R. Peng, F. Gong, Y. Luo, H. Zhang and Q. Cui, *Colloids Surf., A*, 2022, **645**, 128934.
9 P. Maity, S. Takano, S. Yamazoe, T. Wakabayashi and T. Tsukuda, *J. Am. Chem. Soc.*, 2013, **135**, 9450–9457.
10 X. Wan, W. W. Xu, S. Yuan, Y. Gao, X. Zeng and Q. Wang, *Angew. Chem., Int. Ed.*, 2015, **54**, 9683–9686.
11 Q. Xu, S. Wang, Z. Liu, G. Xu, X. Meng and M. Zhu, *Nanoscale*, 2013, **5**, 1176–1182.
12 D. M. Chevrier, X. Meng, Q. Tang, D. Jiang, M. Zhu, A. Chatt and P. Zhang, *J. Phys. Chem. C*, 2014, **118**, 21730–21737.
13 R. R. Nasaruddin, T. Chen, N. Yan and J. Xie, *Coord. Chem. Rev.*, 2018, **368**, 60–79.
14 B. Zhang, J. Chen, Y. Cao, O. J. H. Chai and J. Xie, *Small*, 2021, **17**, 2004381.
15 L. Shang, R. M. Dörlich, S. Brandholt, R. Schneider, V. Trouillet, M. Bruns, D. Gerthsen and G. U. Nienhaus, *Nanoscale*, 2011, **3**, 2009–2014.
16 X. Jiang, X. Wang, C. Yao, S. Zhu, L. Liu, R. Liu and L. Li, *J. Phys. Chem. Lett.*, 2019, **10**, 5237–5243.

17 D. Jiang, M. Kühn, Q. Tang and F. Weigend, *J. Phys. Chem. Lett.*, 2014, **5**, 3286–3289.
18 C. Zeng, H. Qian, T. Li, G. Li, N. L. Rosi, B. Yoon, R. N. Barnett, R. L. Whetten, U. Landman and R. Jin, *Angew. Chem., Int. Ed.*, 2012, **51**, 13114–13118.
19 M. Agrachev, S. Antonello, T. Dainese, M. Ruzzi, A. Zoleo, E. Aprà, N. Govind, A. Fortunelli, L. Sementa and F. Maran, *ACS Omega*, 2017, **2**, 2607–2617.
20 S. Malola and H. Häkkinen, *J. Am. Chem. Soc.*, 2019, **141**, 6006–6012.
21 S. H. Yau, O. Varnavski, J. D. Gilbertson, B. Chandler, G. Ramakrishna and T. Goodson, *J. Phys. Chem. C*, 2010, **114**, 15979–15985.
22 G. Li and R. Jin, *J. Am. Chem. Soc.*, 2014, **136**, 11347–11354.
23 Y. Li, Y. Chen, S. D. House, S. Zhao, Z. Wahab, J. C. Yang and R. Jin, *ACS Appl. Mater. Interfaces*, 2018, **10**, 29425–29434.
24 K. Isozaki, K. Iseri, R. Saito, K. Ueda and M. Nakamura, *Angew. Chem., Int. Ed.*, 2024, **63**, e202312135.
25 X. Zhang, J. Chen, Z. Luo, D. Wu, X. Shen, S. Song, Y. Sun, P. Liu, J. Zhao, S. Huo, S. Fan, F. Fan, X. Liang and J. Xie, *Adv. Healthcare Mater.*, 2014, **3**, 133–141.
26 S. K. Katla, J. Zhang, E. Castro, R. A. Bernal and X. Li, *ACS Appl. Mater. Interfaces*, 2018, **10**, 75–82.
27 P. Huang, J. Lin, S. Wang, Z. Zhou, Z. Li, Z. Wang, C. Zhang, X. Yue, G. Niu, M. Yang, D. Cui and X. Chen, *Biomaterials*, 2013, **34**, 4643–4654.
28 A. Yahia-Ammar, D. Sierra, F. Mérola, N. Hildebrandt and X. L. Guével, *ACS Nano*, 2016, **10**, 2591–2599.
29 J. Singh, N. K. Alruwaili, A. Aodah, W. H. Almalki, S. S. Almujri, M. Alrobaian, S. O. Rab, A. A. Alanezi, E. M. Haji, M. A. Barkat, A. Sahoo, J. A. Lal and M. Rahman, *J. Drug Delivery Sci. Technol.*, 2025, **105**, 106594.
30 C. Amiens, B. Chaudret, D. Ciuculescu-Pradines, V. Collière, K. Fajerwerg, P. Fau, M. Kahn, A. Maisonnat, K. Soulantica and K. Philippot, *New J. Chem.*, 2013, **37**, 3374.
31 J. García-Barrasa, J. M. López-de-Luzuriaga, M. Monge, K. Soulantica and G. Viau, *J. Nanopart. Res.*, 2011, **13**, 791–801.
32 J. M. López-de-Luzuriaga, M. Monge, J. Quintana and M. Rodríguez-Castillo, *Nanoscale Adv.*, 2021, **3**, 198–205.
33 J. Crespo, J. M. López-de-Luzuriaga, M. Monge, M. E. Olmos, M. Rodríguez-Castillo, B. Cormary, K. Soulantica, M. Sestu and A. Falqui, *Chem. Commun.*, 2015, **51**, 16691–16694.
34 A. Guerreiro, I. Compañón, F. S. Lazaris, C. Labão-Almeida, P. Oroz, M. Ghirardello, M. C. Marques, F. Corzana and G. J. L. Bernardes, *Angew. Chem., Int. Ed.*, 2024, **63**, e202411009.
35 Y. Negishi, K. Nobusada and T. Tsukuda, *J. Am. Chem. Soc.*, 2005, **127**, 5261–5270.
36 G. A. Simms, J. D. Padmos and P. Zhang, *J. Chem. Phys.*, 2009, **131**, 214703.
37 Y. Ishida, I. Akita, T. Sumi, M. Matsubara and T. Yonezawa, *Sci. Rep.*, 2016, **6**, 29928.
38 P. Zhang, *J. Phys. Chem. C*, 2014, **118**, 25291–25299.
39 J. Oliver-Meseguer, I. Dominguez, R. Gavara, A. Doménech-Carbó, J. M. González-Calbet, A. Leyva-Pérez and A. Corma, *Chem. Commun.*, 2017, **53**, 1116–1119.
40 L. E. Marbella and J. E. Millstone, *Chem. Mater.*, 2015, **27**, 2721–2739.
41 M. Dasog, W. Hou and R. W. J. Scott, *Chem. Commun.*, 2011, **47**, 8569–8571.
42 H. Yamamoto, H. Yano, H. Kouchi, Y. Obora, R. Arakawa and H. Kawasaki, *Nanoscale*, 2012, **4**, 4148–4154.
43 J. Li, R. R. Nasaruddin, Y. Feng, J. Yang, N. Yan and J. Xie, *Chem.–Eur. J.*, 2016, **22**, 14816–14820.
44 R. Fenger, E. Fertitta, H. Kirmse, A. F. Thünemann and K. Rademann, *Phys. Chem. Chem. Phys.*, 2012, **14**, 9343–9349.
45 E. Seo, J. Kim, Y. Hong, Y. S. Kim, D. Lee and B.-S. Kim, *J. Phys. Chem. C*, 2013, **117**, 11686–11693.
46 X. Cui, Q. Ruan, X. Zhuo, X. Xia, J. Hu, R. Fu, Y. Li, J. Wang and H. Xu, *Chem. Rev.*, 2023, **123**, 6891–6952.
47 Y. Xie, W. Zheng and X. Jiang, *ACS Appl. Mater. Interfaces*, 2020, **12**, 9041–9049.
48 P. Liu, W. Yang, L. Shi, H. Zhang, Y. Xu, P. Wang, G. Zhang, W. R. Chen, B. Zhang and X. Wang, *J. Mater. Chem. B*, 2019, **7**, 6924–6933.
49 Q. Dan, D. Hu, Y. Ge, S. Zhang, S. Li, D. Gao, W. Luo, T. Ma, X. Liu, H. Zheng, Y. Li and Z. Sheng, *Biomater. Sci.*, 2020, **8**, 973–987.
50 Q. Dan, Z. Yuan, S. Zheng, H. Ma, W. Luo, L. Zhang, N. Su, D. Hu, Z. Sheng and Y. Li, *Pharmaceutics*, 2022, **14**, 1645.